Direct Observation of Carbon Dioxide Electroreduction on Gold: Site Blocking by the Stern Layer Controls CO_2 Adsorption Kinetics

Spencer Wallentine, Savini Bandaranayake, Somnath Biswas, and L. Robert Baker*
Department of Chemistry and Biochemistry, The Ohio State University, Columbus, OH 43210
Received September 11, 2020; E-mail: baker.2364@osu.edu

Abstract: Directly observing active surface intermediates represents a major challenge in electrocatalysis, especially for CO_2 electroreduction on Au. We use in-situ, plasmon-enhanced vibrational sum frequency generation spectroscopy, which has detection limits <1% of a monolayer and can access the Au/electrolyte interface during active electrocatalysis in the absence of mass transport limitations. Measuring the potential dependent surface coverage of atop CO confirms that the rate determining step for this reaction is CO_2 adsorption. Analysis of the interfacial electric field reveals the formation of a dense cation layer at the electrode surface, which is correlated to the onset of CO production. The Tafel slope increases in conjunction with the field saturation due to active site blocking by adsorbed cations. These findings show that CO_2 reduction is extremely sensitive to the potential dependent structure of the electrochemical double layer and provides direct observation of the interfacial processes that govern these kinetics.

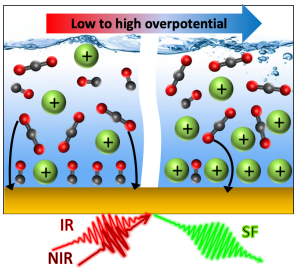

Electrochemical reactions play a pivotal role in batteries,[1–3] photovoltaics,[4–6] fuel cells,[7–9] corrosion,[10,11] and catalysis.[12–15] However, many fundamental processes at electrode/electrolyte interfaces are still not fully understood. For example, during carbon dioxide reduction (CO_2R) on Au electrodes the rate determining step (RDS) has been the subject of debate.[16–19] Despite significant work in this area, direct observation of the Au/electrolyte interface as a function of applied potential is still required to address many outstanding questions in CO_2R electrocatalysis, such as the identity of the RDS and the effect of the potential-dependent electrochemical double layer on the kinetics of this process.[17–20]

In-situ spectroscopy can inform these questions by providing the ability to directly observe surface reaction intermediates.[21–26] A number of groups have tried to measure the potential dependent surface population of *CO (an asterisk indicates a surface bound species) during CO_2R on Au using surface enhanced infrared absorption spectroscopy (SEIRAS), but have been unable to observe it under catalytic conditions.[16,17] To circumvent this challenge, detection often requires production of CO at applied negative potential followed by a positive potential step where accumulated CO binds more efficiently to the electrode surface.[17] Unfortunately, this approach precludes the ability to measure the potential dependent surface coverage of the active species, which is necessary to understand the kinetics that underlie the RDS. Oberst et al.[16,27] were able to see *CO on Au during CO_2R using surface enhanced Raman spectroscopy (SERS), but only in the presence of organic additives, which served to increase the local concentration of CO_2.

Another technique with inherent interface specificity and high sensitivity is vibrational sum frequency generation (VSFG) spectroscopy. We have developed a plasmon-enhnanced VSFG technique which enables direct observation of surface species with detection limits below 1% of a monolayer and is compatible with aqueous electrochemical reactions at high catalytic current densities.[28] This method is necessary to enable direct observation of CO_2 reduction on Au because the catalytic surface population of *CO is very low under steady state turnover on Au electrodes, on the order of only a few percent of a monolayer.[17,19,29,30] Here we use this method to measure the surface coverage and Stark shift of *CO on Au during electrochemical CO_2R as a function of electrode potential. Huang-fu et al. also recently reported potential-dependent VSFG spectra of CO on Au using a front side geometry.[31] However, in such a geometry the ultrathin electrolyte layer (<50 μm) introduces significant mass transport limitations to the spectroelectrochemical cell such that local CO concentration under polarizing bias may be much greater compared to an electrode surface under typical steady state operations. This is a significant advantage of the plasmon-enhanced VSFG method employed here,[28] which probes the electrode surface in the presence of an actively-purged bulk electrolyte, where surface concentrations are not limited by artificial mass transport restrictions (see supporting information section 2). The results of these measurements confirm hypotheses based on micro-kinetic modeling that CO_2 adsorption is rate limiting in this reaction and that the kinetics of CO_2 adsorption are extremely sensitive to the potential dependent structure of the electrochemical double layer.[19]

Figure 1a shows potential-dependent VSFG spectra measured from 2,000-2,200 cm^{-1} during electrochemical CO_2 reduction on polycrystalline Au electrodes in 0.1 M sodium bicarbonate. The cathodic scan starts from 0.4 V at the bottom of Figure 1a, and moving up shows the spectral progression as potential is decreased to -1.5 V and then gradually returned to 0.4 V. Some residual signal from pre-reaction CV cycling can be seen at potentials more positive than the onset potential, but this represents only 3.5% of the total measured signal. Similar measurements obtained on an electrode without prior CV cycling show no detectable CO before the reaction onset (see supporting information sec-

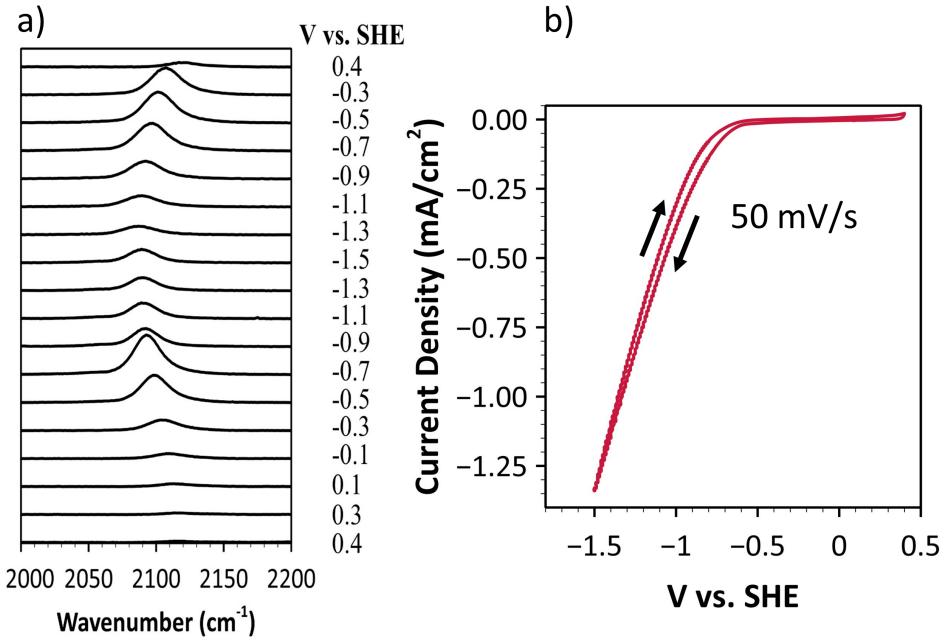

Figure 1. a) In-situ suppressed spectra from atop *CO during catalytic CO_2 conversion. b) Typical cyclic voltammogram obtained during in-situ measurements.

tion 2) confirming that the CO measured here is a result of CO_2 reduction and not trace CO impurities. A cylcic voltammogram corresponding to the potentials in Figure 1a is shown in Figure 1b. The observed peak has a frequency that ranges from 2,116-2,088 cm^{-1} and is indicative of CO bound to an Au surface in the atop position.[16,17,27] The peak frequency changes with potential due to the electrochemical Stark effect. Dipole-dipole coupling can also shift the peak frequency. We can quantitatively account for dipole-dipole coupling, and this analysis is shown in the supporting information section 3. We find that dipole-dipole coupling represents a negligible contribution to the observed frequency shift due to the very low coverage of CO on the Au surface (see sections 4 and 3 of the supporting information for a detailed analysis of surface coverage and dipole-dipole coupling). The intensity also shows an interesting potential dependence.

In order to understand how the relative intensity and Stark shift of the observed *CO informs the surface reaction kinetics, we consider the following elementary reaction steps for CO_2R on Au:[19]

$$CO_{2(g)} \text{ Mass transport} \quad (1)$$

$$CO_{2(g)} + e^- \rightleftharpoons {}^*CO_2{}^- \quad (2)$$

$${}^*CO_2{}^- + H^+_{(aq)} \rightleftharpoons {}^*COOH \quad (3)$$

$${}^*COOH + H^+_{(aq)} + e^- \rightleftharpoons {}^*CO + H_2O_{(l)} \quad (4)$$

$${}^*CO \rightleftharpoons CO_{(g)} \quad (5)$$

At catalytic current densities, a pH gradient near the electrode surface is expected based on the consumption of protons by a combination of CO_2R and HER. Under these conditions, it has been hypothesized that the rates of reactions 3 and 4 above will limit the overall CO_2R rate as mediated by a combination of proton diffusion as well as the buffering capacity of the electrolyte.[17,32–36] Other studies have shown that the rate of CO_2R is insensitive to reaction pH, indicating rather that the RDS does not involve protons.[16,19,37] This observation argues instead that CO_2 adsorption (reaction 2) is rate determining for all values of applied potential until the mass transport regime.[16,18,37–39] However, assuming a single RDS that does not change with potential makes it difficult to reconcile the potential-dependent Tafel slope commonly observed for CO_2R.[16,18,19,37–39]

To consider this question, Figure 2 shows the intensity profile of *CO at different potentials for a positive and negative potential scan (compilation of multiple experiments). Here *CO intensity is plotted on a square root scale so as to be proportional to absolute surface coverage, ignoring third order contributions as addressed below. Using peak area calibrated to a known coverage of a 4-mercaptobenzonitrile on Au, we have estimated the potential dependent absolute surface coverage of *CO on Au, and these estimates are provided in section 4 of the supporting information. We note

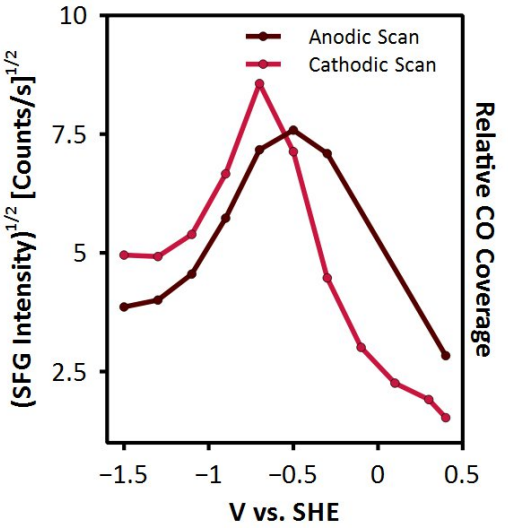

Figure 2. Relative coverage as a function of potential. Here the square root of the *CO peak intensity is plotted, which is proportional to the absolute coverage.

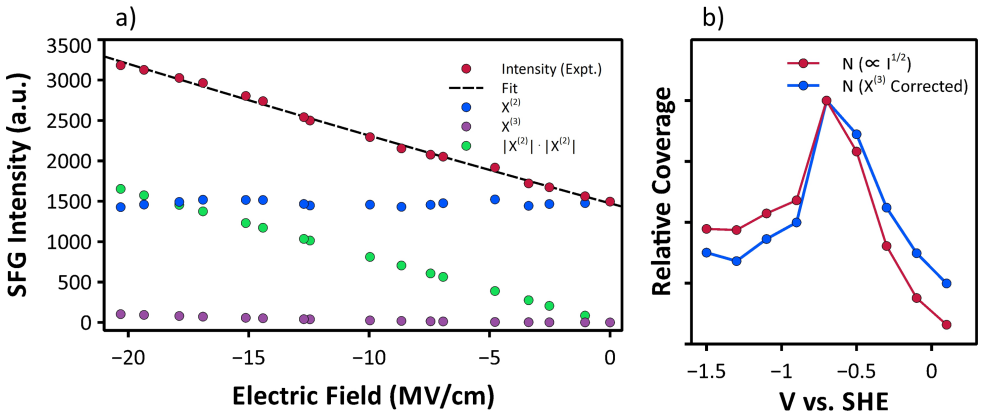

Figure 3. a) Deconvolution of the contribution of $\chi^{(2)}$, $\chi^{(2)}\dot{\chi}^{(3)}$, and $\chi^{(3)}$ to the SFG intensity of a 4-mercaptobenzonitrile SAM. b) Normalized relative CO coverage as measured, and with corrections for third order contributions assuming a $\chi^{(3)}/\chi^{(2)}$ ratio of 2.3.

that the highest coverage occurs at -0.7 V and represents approximately 4.9 % of a monolayer. This low coverage is a consequence of weak binding to Au, and is consistent with both experimental and theoretical data.[17,19,29,30] As the potential is scanned to negative potentials, the intensity of the *CO peak initially increases until somewhere between -0.7 and -0.9 V, where it drops sharply and levels off by -1.2 V. During the anodic scan, the *CO peak intensity is reversible and recovers as the potential is returned to more positive potentials. In the anodic scan the peak maximum appears to shift to less negative potentials. This behavior is a result of *CO persisting on the electrode surface during the anodic scan, which is not present in the cathodic scan.

This analysis is based on the assumption that the measured signal originates from the second order non-linear susceptibility ($\chi^{(2)}$) and is proportional to the square of surface population. However, it has been shown that when the interfacial electric field is on the order of tens of MV/cm as is the case here, third order (i.e. $\chi^{(3)}$) contributions can contribute to the measured signal.[40,41] To carefully account for the possibility of third order contributions in this analysis, we have quantified the ratio of $\chi^{(3)}/\chi^{(2)}$ by measuring the potential-dependent VSFG signal from a self-assembled monolayer of 4-mercaptobenzonitrile on Au, over a range where surface coverage is constant with potential. Figure 3a shows this analysis, and the associated equations and fitting parameters are given in the supporting information section 5. We find the $\chi^{(3)}/\chi^{(2)}$ ratio is $2.3 \pm 0.4 \times 10^{-10}$ m V^{-1}, which is within error of the previously reported value for a related system.[41] Assuming a similar relative $\chi^{(3)}$ value for in-situ generated *CO on Au, we are able to deconvolute the second and third order contributions to the measured CO intensity profile. The results are show in Figure 3b and confirm that the relative surface coverage of *CO shows an almost identical potential profile when $\chi^{(3)}$ is quantitatively accounted for, indicating that these conclusions are robust to possible third order contributions to the measured VSFG signal.

A decrease in surface coverage indicates a rate reduction for one or more elementary steps depicted in reactions 2-4, an increase in reaction 5, and/or a loss of active surface sites. While a number of theoretical studies have treated CO desorption as potential-independent,[19,42] spectroscopic studies indicate that CO adsorption/desorption kinetics are complex and may vary with applied potential.[16,17,43] This decrease in *CO surface population could be caused by a rate reduction in reactions 3 or 4 as protons are consumed at higher current densities as has been postulated.[32,36] However, this could also be caused by site blocking by cations, which adsorb on the electrode surface at negative potentials and can limit the rate of CO_2 adsorption.[17,32,44] Below we show by analysis of the Stark tuning curve for *CO that the electric field in the Stern layer saturates as a function of applied potential, indicating the formation of a densely packed cation layer on the electrode surface. This saturation occurs at the same potential where we observe a decrease in the *CO peak intensity. These observations provide strong spectroscopic evidence that site blocking by adsorbed cations mediates access to the surface and directly supports predictions based on microkinetic models confirming that CO_2 adsorption kinetics are extremely sensitive to the potential-dependent structure of the electric double layer.[19]

Figure 4a shows the CO peak frequency as a function of applied potential. The Stark tuning rate for the linear region is $\sim$19 cm^{-1}/V which is similar to other values reported by VSFG for CO complexes on Au electrodes.[25] The frequency shift from *CO can be used to deduce the magnitude of the interfacial field using Equation 6.[45]

$$\omega(\phi) = \omega_0 - \vec{\Delta\mu} \cdot \vec{F}(\phi) \tag{6}$$

Here $\omega(\phi)$ is the potential dependent peak frequency, $\vec{\Delta\mu}$ is the vector that describes the orientation of the infrared dipole and its dipole difference due to an applied field, and $\vec{F}(\phi)$ is the potential dependent electric field vector. The zero field frequency, ω_0, is the Stark frequency when the electrode surface is at its zero charge potential. For polycrystalline Au electrodes the potential-of-zero-charge (pzc) occurs at 0.08 V vs SHE as determined by the capacitance minimum obtained using electrochemical impedance (see supporting information section 6). Using the value of 0.7 $cm^{-1}/(MV/cm)$ for $\vec{\Delta\mu}$[46] and assuming the dipole and field are on average oriented normal to the surface, the interfacial electric field is calculated and is given in Figure 4b. These fields are on the same order as have been observed previously for similar systems.[25,26,45]

We also collected stark tuning curves using the CN stretch of 4-mercaptobenzonitrile, a common Stark reporter (Figure 4a).[26,47] The experimental spectra are shown in the supporting information (section 7) as is the impedance data which

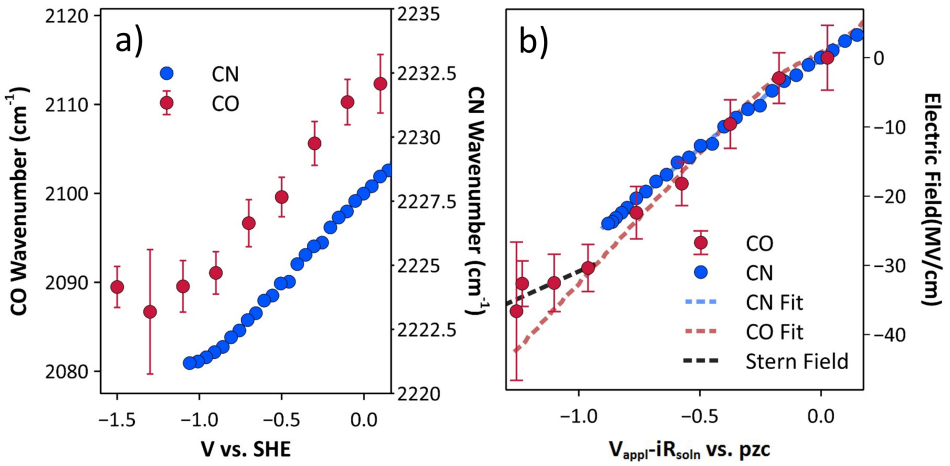

Figure 4. a) Potential dependent frequencies for CO and CN stark reporters. b) Ohmic drop corrected potential (V_{appl}-iR_{soln}) and the corresponding electric field calculated from Equation 6. The CN and CO fit show a best fit line calculated with Guoy-Chapman-Stern theory. The Stern field is a liner fit to the points below -0.9 V. Error bars represent standard deviations from replicate measurements.

show a pzc for this functionalized surface of 0.0 V vs SHE (section 6). This molecule is known to exhibit a tilt angle of 40° when adsorbed on Au, and this has been accounted for in the dot product of the dipole moment with the electric field vector as shown in Equation 6.[48] The value for $1/\vec{\Delta\mu}$ of 0.36 $(MV/cm)/cm^{-1}$ is given by Shi et al.[26] This study also investigated the effect of solvation on frequency shifts of Stark reporters. By comparing the stretching frequency in air with that in aqueous electrolyte measured at the pzc, they calculate the change in frequency due to solvation at a fixed potential. For the CN reporter, the frequency is blue shifted in water relative to air by ∼0.25 cm^{-1}. Here we account for solvation effects by referencing the Stark tuning curves for both CN and CO to the experimentally measured pzc.

As shown in Figure 4a, the electric field saturates at more negative potentials. This has been observed before,[25] and Patrow et al.[49] propose that this occurs when the electrode reaches a steady state polarization due to the Faradaic current associated here with CO_2R and HER. It is possible to correct for this potential drop by using electrochemical impedance to measure the electrolyte ohmic drop as a function of applied potential.[26,47–50] We use this method to obtain the corrected data for both CO and CN Stark reporters as shown in Figure 4b. Also shown in the figure are fits using the Gouy-Chapman-Stern model (see supporting information section 8).

Analysis of these data show that while these two reporters experience similar interfacial electric fields, the 4-mercaptobenzonitrile Stark reporter is unable to measure the field at potentials relevant to CO_2R due to irreversible reductive desorption of the thiol at potentials more negative than -1 V (see supplementary figure S6). Additionally, while correcting for ohmic drop linearizes the CN data, the *CO data still shows saturation of the electric field at potentials more negative than -0.9 V indicating that the potential decrease due to ohmic drop does not fully account for this effect. This behavior results from the Stern layer, and indicates that the Stern layer field is saturating due to formation of a dense cation layer at the Au/electrolyte interface. This observation indicates a site blocking mechanism, where a dense cation layer limits the kinetics of CO_2 adsorption as described above.[17,51] We note that the drop in *CO intensity occurs between -0.7 and -0.9 V and exactly matches the potential for formation of a dense Stern layer as shown in Figure 4b.

The decrease in *CO at potentials more negative than -0.9 V shown in Figure 2 is also correlated to a change in the Tafel slope and the onset for high faradaic efficiency CO production observed previously.[18,19,29,38] Both of these observables are consistent with our data. First, the Tafel slope for potentials less negative than -0.9 V vs SHE is commonly reported as ∼118 mV/decade, consistent with a one electron reduction of CO_2 to CO_2^-.[16,18,19,37–39] However, at more negative potentials, the Tafel slope increases and approaches infinity.[18,19] The Tafel slope is derived from fundamental rate laws, and for the case where CO_2 adsorption is rate limiting, this slope is given by Equation 7:[52]

$$\frac{\partial log j_{CO}}{\partial E} = -\frac{\beta F}{2.3RT} + \frac{\partial log\theta}{\partial E} \tag{7}$$

where j_{CO} is the partial current density to CO, E is the potential, β is the symmetry factor and is typically set to 0.5, F is Faraday's constant, R is the gas constant, T is the temperature, and θ is the active site coverage.

For simplicity, θ is often approximated to be unity. However, our observation of site blocking by the potential-dependent Stern layer nullifies this approximation, and accounting for this term explains the increasing Tafel slope as free active sites are blocked by adsorbed cations. While Tafel plots typically show some curvature at potentials more negative than -0.7 V, the slope can be approximated in a given potential region. Between -0.9 and -1.2 V the slope is ∼300 mV/decade.[18] Using this value and assuming that the one electron reduction of CO_2 to CO_2^- is the RDS, the active site coverage over this potential range is calculated to be ∼3%. We note that this value is in very close agreement with the measured surface coverage of *CO, which is approximated to be 3.2% at -1.1 V (see supporting information section 4). This analysis, which explains the potential dependent Tafel slope based on changes in the active site density, is corroborated here by the direct observation that potential-induced cation adsorption controls the availability of active sites for CO_2 adsorption. Additionally, the formation of a dense Stern layer by -0.9 V vs SHE corresponds with the well-established onset for CO_2R and is consistent with recent reports that the presence of alkali cations on

the electrode surface enhances CO_2R reaction kinetics by lowering the activation barrier due to formation of a strong interfacial electric field.[33,42]

Interestingly, the observed decrease in population and saturation of the Stern layer are correlated to the onset of efficient CO_2R, which suggests that the observed surface population is not directly correlated with activity.[16,18] These results can be interpreted in the context of leading research by Norskov and Sargent who show that the strong electric field generated near an adsorbed cation results in a significantly enhanced reaction rate for CO_2 reduction.[33,42] Consequently, the increased overall reaction rate indicates that although cations block the majority of surface sites, those few sites remaining are highly active. In fact, this can be taken as direct experimental evidence that cation adsorption significantly enhances local reactivity as theoretically predicted. Modeling by Liu et al.[33] suggests that the resonance time of CO_2 decreases as the surface cation concentration increases. As we measure a time averaged coverage, if the resonance time decreases, the time averaged intensity will also be expected to decrease as observed.

Recent work by Li et al.[24] have investigated the role of interfacial solvation on CO_2R selectivity on Cu and find that hydrogen bonding plays a role in steering product selectivity. While the structure of interfacial water on Au electrodes has been the subject of numerous studies,[53–57] much remains to be learned about the effects of interfacial solvation on electrochemical kinetics. The potential-dependent adsorption of cations is expected to influence the interfacial water structure,[58,59] and the correlation between this structure and CO_2R kinetics remains the subject of ongoing work.

These results represent direct observation of an active electrochemical interface during CO_2R. Using the potential dependent intensity and electric field reported by $^*CO$ during steady state electrolysis, we provide direct evidence for the correlation between formation of a dense Stern layer,CO_2 adsorption, and the onset of CO_2R activity. These observations provide new insight into the interfacial processes that control the kinetics of this important catalytic reaction.

Supporting Information

The supporting material contains information on the 1. Experimental details 2. Steady state population of $^*CO$ 3. Frequency shifts due to dipole-dipole coupling 4. $^*CO$ surface coverage 5. Contributions of $\chi^{(2)}$ and $\chi^{(3)}$ to the VSFG intensity. 6. Double layer capacitance and potential of zero charge 7. VSFG spectra of 4-mercaptobenzonitrile as a function of electrode potential and 8. Gouy-Chapman-Stern model.

Acknowledgements

This work was supported by National Science Foundation under under NSF award number 1665280. XPS was performed at the OSU Surface Analysis Laboratory. Film deposition was performed at the OSU Nanosystems Laboratory. We thank the OSU College of Arts and Sciences machine shops for their help in fabrication of the VSFG system and electrochemical cell. We thank Dr. Anne Co for assistance with electrochemical impedance measurements.

References

(1) Peng, Z.; Freunberger, S. A.; Chen, Y.; Bruce, P. G. A reversible and higher-rate Li-O_2 battery. *Science* **2012**, *337*, 563–566.
(2) Manthiram, A.; Fu, Y.; Su, Y.-S. Challenges and prospects of lithium–sulfur batteries. *Acc. Chem. Res.* **2012**, *46*, 1125–1134.
(3) Cheng, F.; Chen, J. Metal–air batteries: from oxygen reduction electrochemistry to cathode catalysts. *Chem. Soc. Rev.* **2012**, *41*, 2172–2192.
(4) Khaselev, O.; Turner, J. A. A monolithic photovoltaic-photoelectrochemical device for hydrogen production via water splitting. *Science* **1998**, *280*, 425–427.
(5) Heller, A. Conversion of sunlight into electrical power and photoassisted electrolysis of water in photoelectrochemical cells. *Acc. Chem. Res.* **1981**, *14*, 154–162.
(6) Winkler, M. T.; Cox, C. R.; Nocera, D. G.; Buonassisi, T. Modeling integrated photovoltaic–electrochemical devices using steady-state equivalent circuits. *Proc. Natl. Acad. Sci. U.S.A.* **2013**, *110*, E1076–E1082.
(7) Yilanci, A.; Dincer, I.; Ozturk, H. K. A review on solar-hydrogen/fuel cell hybrid energy systems for stationary applications. *Prog. Energy Combust. Sci.* **2009**, *35*, 231–244.
(8) Minh, N. Q. Solid oxide fuel cell technology—features and applications. *Solid State Ionics* **2004**, *174*, 271–277.
(9) Winter, M.; Brodd, R. J. What are batteries, fuel cells, and supercapacitors? *Chem. Rev.* **2004**, *104*, 4245–4270.
(10) Zhong, C.; Tang, X.; Cheng, Y. Corrosion of steel under the defected coating studied by localized electrochemical impedance spectroscopy. *Electrochim. Acta* **2008**, *53*, 4740–4747.
(11) Cole, I. S.; Marney, D. The science of pipe corrosion: A review of the literature on the corrosion of ferrous metals in soils. *Corros. Sci.* **2012**, *56*, 5–16.
(12) Savéant, J.-M. Molecular catalysis of electrochemical reactions. Mechanistic aspects. *Chem. Rev.* **2008**, *108*, 2348–2378.
(13) Jutand, A. Contribution of electrochemistry to organometallic catalysis. *Chem. Rev.* **2008**, *108*, 2300–2347.
(14) Fabbri, E.; Habereder, A.; Waltar, K.; Kötz, R.; Schmidt, T. J. Developments and perspectives of oxide-based catalysts for the oxygen evolution reaction. *Catal. Sci. Technol.* **2014**, *4*, 3800–3821.
(15) Zheng, Y.; Jiao, Y.; Zhu, Y.; Li, L. H.; Han, Y.; Chen, Y.; Du, A.; Jaroniec, M.; Qiao, S. Z. Hydrogen evolution by a metal-free electrocatalyst. *Nat. Commun.* **2014**, *5*, 3783.
(16) Wuttig, A.; Yaguchi, M.; Motobayashi, K.; Osawa, M.; Surendranath, Y. Inhibited proton transfer enhances Au-catalyzed CO2-to-fuels selectivity. *Proc. Natl. Acad. Sci. U. S. A.* **2016**, *113*, E4585–E4593.
(17) Dunwell, M.; Lu, Q.; Heyes, J. M.; Rosen, J.; Chen, J. G.; Yan, Y.; Jiao, F.; Xu, B. The central role of bicarbonate in the electrochemical reduction of carbon dioxide on gold. *J. Am. Chem. Soc.* **2017**, *139*, 3774–3783.
(18) Zhang, B. A.; Ozel, T.; Elias, J. S.; Costentin, C.; Nocera, D. G. Interplay of homogeneous reactions, mass transport, and kinetics in determining selectivity of the reduction of CO_2 on gold electrodes. *ACS Cent. Sci.* **2019**, *5*, 1097–1105.
(19) Ringe, S.; Morales-Guio, C. G.; Chen, L. D.; Fields, M.; Jaramillo, T. F.; Hahn, C.; Chan, K. Double layer charging driven carbon dioxide adsorption limits the rate of electrochemical carbon dioxide reduction on Gold. *Nat. Commun.* **2020**, *11*, 1–11.
(20) Willets, K. A.; Van Duyne, R. P. Localized surface plasmon resonance spectroscopy and sensing. *Annu. Rev. Phys. Chem.* **2007**, *58*, 267–297.
(21) Neri, G.; Donaldson, P. M.; Cowan, A. J. The role of electrode–catalyst interactions in enabling efficient CO_2 reduction with Mo (bpy)(CO) 4 as revealed by vibrational sum-frequency generation spectroscopy. *J. Am. Chem. Soc.* **2017**, *139*, 13791–13797.
(22) Herlihy, D. M.; Waegele, M. M.; Chen, X.; Pemmaraju, C.; Prendergast, D.; Cuk, T. Detecting the oxyl radical of photocatalytic water oxidation at an n-$SrTiO_3$/aqueous interface through its subsurface vibration. *Nat. Chem.* **2016**, *8*, 549.
(23) Gardner, A.; Khezar, S.; Cowan, A. J. Vibrational sum-frequency generation spectroscopy of electrode surfaces: studying the mechanisms of sustainable fuel generation and utilisation. *Phys. Chem. Chem. Phys.* **2019**, *21*, 12067–12086.
(24) Li, J.; Li, X.; Gunathunge, C. M.; Waegele, M. M. Hydrogen bonding steers the product selectivity of electrocatalytic CO reduction. *Proc. Natl. Acad. Sci. U. S. A.* **2019**, *116*, 9220–9229.
(25) Clark, M. L.; Ge, A.; Videla, P. E.; Rudshteyn, B.; Miller, C. J.; Song, J.; Batista, V. S.; Lian, T.; Kubiak, C. P. CO_2 reduction catalysts on gold electrode surfaces influenced by large electric fields. *J. Am. Chem. Soc.* **2018**, *140*, 17643–17655.
(26) Shi, H.; Cai, Z.; Patrow, J.; Zhao, B.; Wang, Y.; Wang, Y.; Benderskii, A.; Dawlaty, J.; Cronin, S. B. Monitoring local electric fields at electrode surfaces using surface enhanced raman scattering-based stark-shift spectroscopy during hydrogen evolution reactions. *ACS Appl. Mater. Interfaces* **2018**, *10*, 33678–33683.
(27) Oberst, J. L.; Kenis, P.; Jhong, H.; Gewirth, A. A. Insight into the electrochemical reduction of CO_2 on gold via surface-

enhanced Raman spectroscopy and N-containing additives. *J. Solid State Electrochem.* **2016**, *20*, 1149–1154.
(28) Wallentine, S.; Bandaranayake, S.; Biswas, S.; Baker, L. R. Plasmon-resonant vibrational sum frequency generation of electrochemical interfaces: Direct observation of carbon dioxide electroreduction on gold. *J. Phys. Chem. A (Online early access) DOI:doi:10.1021/acs.jpca.0c04268.* Published Online Aug 26, 2020, accessed Aug 27, 2020 (accepted manuscript, has not undergone final copyediting, typesetting, or proof review).
(29) Cave, E. R.; Montoya, J. H.; Kuhl, K. P.; Abram, D. N.; Hatsukade, T.; Shi, C.; Hahn, C.; Nørskov, J. K.; Jaramillo, T. F. Electrochemical CO_2 reduction on Au surfaces: mechanistic aspects regarding the formation of major and minor products. *Phys. Chem. Chem. Phys.* **2017**, *19*, 15856–15863.
(30) Katayama, Y.; Nattino, F.; Giordano, L.; Hwang, J.; Rao, R. R.; Andreussi, O.; Marzari, N.; Shao-Horn, Y. An in situ surface-enhanced infrared absorption spectroscopy study of electrochemical CO_2 reduction: selectivity dependence on surface C-bound and O-bound reaction intermediates. *J. Phys. Chem. C* **2018**, *123*, 5951–5963.
(31) Huang-Fu, Z.-C.; Song, Q.-T.; He, Y.-H.; Wang, J.-J.; Ye, J.-Y.; Zhou, Z.-Y.; Sun, S.-G.; Wang, Z.-H. Electrochemical CO_2 reduction on Cu and Au electrodes studied using in situ sum frequency generation spectroscopy. *Physical Chemistry Chemical Physics* **2019**, *21*, 25047–25053.
(32) Dunwell, M.; Luc, W.; Yan, Y.; Jiao, F.; Xu, B. Understanding surface-mediated electrochemical reactions: CO_2 reduction and beyond. *ACS Catal.* **2018**, *8*, 8121–8129.
(33) Liu, M.; Pang, Y.; Zhang, B.; De Luna, P.; Voznyy, O.; Xu, J.; Zheng, X.; Dinh, C. T.; Fan, F.; Cao, C. et al. Enhanced electrocatalytic CO 2 reduction via field-induced reagent concentration. *Nature* **2016**, *537*, 382.
(34) Chen, Y.; Li, C. W.; Kanan, M. W. Aqueous CO_2 reduction at very low overpotential on oxide-derived Au nanoparticles. *J. Am. Chem. Soc.* **2012**, *134*, 19969–19972.
(35) Dunwell, M.; Yang, X.; Setzler, B. P.; Anibal, J.; Yan, Y.; Xu, B. Examination of near-electrode concentration gradients and kinetic impacts on the electrochemical reduction of CO_2 using surface-enhanced infrared spectroscopy. *ACS Catal.* **2018**, *8*, 3999–4008.
(36) Yang, K.; Kas, R.; Smith, W. A. In situ infrared spectroscopy reveals persistent alkalinity near electrode surfaces during CO2 electroreduction. *J. Am. Chem. Soc.* **2019**, *141*, 15891–15900.
(37) Wuttig, A.; Yoon, Y.; Ryu, J.; Surendranath, Y. Bicarbonate is not a general acid in Au-catalyzed CO_2 electroreduction. *J. Am. Chem. Soc.* **2017**, *139*, 17109–17113.
(38) Hori, Y.; Murata, A.; Kikuchi, K.; Suzuki, S. Electrochemical reduction of carbon dioxides to carbon monoxide at a gold electrode in aqueous potassium hydrogen carbonate. *J. Chem. Soc., Chem. Commun.* **1987**, 728–729.
(39) Noda, H.; Ikeda, S.; Yamamoto, A.; Einaga, H.; Ito, K. Kinetics of electrochemical reduction of carbon dioxide on a gold electrode in phosphate buffer solutions. *Bull. Chem. Soc. Jpn.* **1995**, *68*, 1889–1895.
(40) Rey, N. G.; Dlott, D. D. Studies of electrochemical interfaces by broadband sum frequency generation. *J. Electroanal. Chem.* **2017**, *800*, 114–125.
(41) Koelsch, P.; Muglali, M. I.; Rohwerder, M.; Erbe, A. Third-order effects in resonant sum-frequency-generation signals at electrified metal/liquid interfaces. *J. Opt. Soc. Am. B* **2013**, *30*, 219–223.
(42) Chen, L. D.; Urushihara, M.; Chan, K.; Nørskov, J. K. Electric field effects in electrochemical CO_2 reduction. *ACS Catal.* **2016**, *6*, 7133–7139.
(43) Wuttig, A.; Liu, C.; Peng, Q.; Yaguchi, M.; Hendon, C. H.; Motobayashi, K.; Ye, S.; Osawa, M.; Surendranath, Y. Tracking a common surface-bound intermediate during CO_2-to-fuels catalysis. *ACS Cent. Sci.* **2016**, *2*, 522–528.
(44) Yamakata, A.; Osawa, M. Destruction of the water layer on a hydrophobic surface induced by the forced approach of hydrophilic and hydrophobic cations. *J. Phys. Chem. Lett.* **2010**, *1*, 1487–1491.
(45) Ge, A.; Videla, P. E.; Lee, G. L.; Rudshteyn, B.; Song, J.; Kubiak, C. P.; Batista, V. S.; Lian, T. Interfacial structure and electric field probed by in situ electrochemical vibrational Stark effect spectroscopy and computational modeling. *J. Phys. Chem. C* **2017**, *121*, 18674–18682.
(46) Fried, S. D.; Boxer, S. G. Measuring electric fields and noncovalent interactions using the vibrational Stark effect. *Acc. Chem. Res.* **2015**, *48*, 998–1006.
(47) Oklejas, V.; Sjostrom, C.; Harris, J. M. SERS detection of the vibrational stark effect from nitrile-terminated SAMs to probe electric fields in the diffuse double-layer. *J. Am. Chem. Soc.* **2002**, *124*, 2408–2409.
(48) Schkolnik, G.; Salewski, J.; Millo, D.; Zebger, I.; Franzen, S.; Hildebrandt, P. Vibrational Stark effect of the electric-field reporter 4-mercaptobenzonitrile as a tool for investigating electrostatics at electrode/SAM/solution interfaces. *Int. J. Mol. Sci.* **2012**, *13*, 7466–7482.
(49) Patrow, J. G.; Sorenson, S. A.; Dawlaty, J. M. Direct spectroscopic measurement of interfacial electric fields near an electrode under polarizing or current-carrying conditions. *J. Phys. Chem. C* **2017**, *121*, 11585–11592.
(50) Sorenson, S. A.; Patrow, J. G.; Dawlaty, J. M. Solvation reaction field at the interface measured by vibrational sum frequency generation spectroscopy. *J. Am. Chem. Soc.* **2017**, *139*, 2369–2378.
(51) Strmcnik, D.; Kodama, K.; van der Vliet, D.; Greeley, J.; Stamenkovic, V. R.; Marković, N. The role of non-covalent interactions in electrocatalytic fuel-cell reactions on platinum. *Nat. Chem.* **2009**, *1*, 466.
(52) Lee, C. W.; Cho, N. H.; Im, S. W.; Jee, M. S.; Hwang, Y. J.; Min, B. K.; Nam, K. T. New challenges of electrokinetic studies in investigating the reaction mechanism of electrochemical CO_2 reduction. *J. Mat. Chem. A* **2018**, *6*, 14043–14057.
(53) Tong, Y.; Lapointe, F.; Thämer, M.; Wolf, M.; Campen, R. K. Hydrophobic water probed experimentally at the gold electrode/aqueous interface. *Angew. Chem. Int. Ed.* **2017**, *56*, 4211–4214.
(54) Li, C.-Y.; Le, J.-B.; Wang, Y.-H.; Chen, S.; Yang, Z.-L.; Li, J.-F.; Cheng, J.; Tian, Z.-Q. In situ probing electrified interfacial water structures at atomically flat surfaces. *Nat. Mater.* **2019**, *18*, 697–701.
(55) Nihonyanagi, S.; Ye, S.; Uosaki, K.; Dreesen, L.; Humbert, C.; Thiry, P.; Peremans, A. Potential-dependent structure of the interfacial water on the gold electrode. *Surf. Sci.* **2004**, *573*, 11–16.
(56) Lin, X.; Groß, A. First-principles study of the water structure on flat and stepped gold surfaces. *Surf. Sci.* **2012**, *606*, 886–891.
(57) Ataka, K.-i.; Osawa, M. In situ infrared study of water- sulfate coadsorption on gold (111) in sulfuric acid solutions. *Langmuir* **1998**, *14*, 951–959.
(58) Waegele, M. M.; Gunathunge, C. M.; Li, J.; Li, X. How cations affect the electric double layer and the rates and selectivity of electrocatalytic processes. *J. Chem. Phys.* **2019**, *151*, 160902.
(59) Hua, W.; Verreault, D.; Huang, Z.; Adams, E. M.; Allen, H. C. Cation effects on interfacial water organization of aqueous chloride solutions. I. Monovalent cations: Li+, Na+, K+, and NH4+. *J. Phys. Chem. B* **2014**, *118*, 8433–8440.